JOURNAL OF SOLID STATE CHEMISTRY 111, 283–293 (1994)

A TEM Study of Defect Ordering in a Calcium Yttrium Sulfide Solid Solution with an Average NaCl-Type Structure

R. L. Withers, L. C. Otero-Diaz,* and J. G. Thompson

*Research School of Chemistry, Australian National University, Canberra, A.C.T, 0200, Australia; and *Quimica Inorganica, F. Quimicas, Universidad Complutense, 28040 Madrid, Spain*

Received May 19, 1993; in revised form September 27, 1993; accepted September 29, 1993

A detailed transmission electron microscope and powder X-ray diffraction study has been made of $Ca_5Y_4S_{11}$, which is one limiting composition of the widely substoichiometric, NaCl-related, solid solution $(1 - x)CaS + (x)\ Y_2S_3$, $0 \leq x \leq 2/7$, in the $CaS–Y_2S_3$ system. Long-range vacancy ordering and associated structural relaxation characterized by the modulation wave vector $\mathbf{q} = \frac{1}{2}(111)^*$ is shown to lower the space group symmetry from cubic to rhombohedral. Twinning between rhombohedral domains and antiphase boundaries within a particular rhombohedral domain are observed as well as a spectacular diffuse intensity distribution which shows many similarities but also significant differences to that previously reported in substoichiometric transition metal carbides and nitrides. © 1994 Academic Press, Inc.

1. INTRODUCTION

Widely sub-stoichiometric solid solutions based upon the NaCl structure type represent a well-known and much studied class of materials. Examples include sub-stoichiometric early transition metal sulfides and selenides (1–5), analogous solid solutions formed from CaS or CaSe via the addition of R_2X_3 chalcogenides of the heavy lanthanides (6–8) along with sub-stoichiometric transition metal carbides and nitrides (9, 10). A characteristic of such solid solution fields is that the nominally vacant sites always occur on only one of the two sub-lattice arrays of the NaCl (B1) structure type, the other sub-lattice array remaining almost completely intact.

Vacancy ordering and associated structural relaxation sometimes leads to sub-solidus superstructure phases (3, 11, 12) within a broader nonstoichiometric composition range as indicated by the existence of extra satellite reflections, at $\mathbf{G} \pm \mathbf{q}$, in addition to the strong Bragg reflections, $\mathbf{G}$, of the underlying $Fm3m$, NaCl-type average structure. Billingham *et al.* (9), for example, report the existence of two sub-solidus ordered phases in the VC_{1-x} system, while a nonstoichiometric $Yb_{1-\delta}S$ phase with doubled cubic lattice parameter has been reported for $Yb_{0.875}S$ (13). The modulation wave-vectors, $\mathbf{q}$, characteristic of such superlattice phases almost invariably include wave-vectors of the form $\frac{1}{2}\{111\}^*$ ($(hkl)^*$ throughout this paper refers to the reciprocal lattice vector $h\mathbf{a}^* + k\mathbf{b}^* + l\mathbf{c}^*$). Thus the space group symmetry proposed for the doubled unit cell of $Yb_{0.875}S$, i.e., $F43m$, allows reflections of the form $\mathbf{G} \pm \frac{1}{2}\{111\}^*$ but not reflections of the form $\mathbf{G} \pm \frac{1}{2}\{110\}^*$ etc. If only one of the four possible modulation wave-vectors of the form $\frac{1}{2}\{111\}^*$ locally exists, as has been reported to be the case for $Sc_{0.80}S$ below 700°C (17), a rhombohedral superstructure (with $\mathbf{a}' = \frac{1}{2}(2\mathbf{a} + \mathbf{b} + \mathbf{c})$, $\mathbf{b}' = \frac{1}{2}(\mathbf{a} + 2\mathbf{b} + \mathbf{c})$, $\mathbf{c}' = \frac{1}{2}(\mathbf{a} + \mathbf{b} + 2\mathbf{c})$) results. Sometimes, in addition, modulation wave-vectors of the form $\sim\frac{2}{3}\{110\}^*$ also condense out (3, 11, 12, 17), leading to more complicated superstructure phases.

The detection and characterization of the local symmetry of such ordered superstructure phases is difficult, however, due to the fact that the underlying average structure cell parameters always remain metrically very close to cubic. Thus Tomas *et al.* (13), for example, in their single crystal X-ray study of $Yb_{0.875}S$, suggest that the local symmetry of this material may well be rhombohedral even though they could index all reflections on the doubled cubic unit cell with space group $F43m$. Slight rhombohedral and monoclinic distortion of the underlying average cell parameters has been detected, however, in several cases (14–16).

In the case of the sub-stoichiometric transition metal carbides and nitrides (9, 10), reciprocal space exhibits a spectacular diffuse intensity distribution (9) due to short-range order and associated structural relaxation when there is no long-range ordering into a superstructure phase. No such diffuse intensity distributions have been reported for the sub-stoichiometric transition metal sulfides or selenides although, in the case of $Sc_{1-x}S$ (17), a $\langle 112 \rangle$ zone axis electron diffraction pattern has been published showing both sharp satellite reflections characteristic of superstructure ordering and diffuse intensity characteristic of short-range order.

The purpose of this contribution is to present the results of a powder XRD and TEM study of such an NaCl-related phase (one whose reciprocal space exhibits both a spec-

0022-4596/94 $6.00

tacular diffuse intensity distribution as well as additional satellite reflections) in the system $(1 - x)CaS + (x)Y_2S_3$. The Ca–Y–S ternary system has been studied by Flahaut and co-workers (6, 7) by X-ray powder diffraction in the temperature range 800–1400°C. These authors report the existence of a widely nonstoichiometric solid solution region with NaCl (B1) structure type of the form $(Ca, Y)_{1-x/3}S$, $x = 0$ to ~0.397 at 1350°C. The unit cell parameter of the average NaCl-type structure was found to vary from 5.64 to 5.69 Å. However, according to Ref. (6) the variation of this unit cell parameter was not linear with composition.

2. EXPERIMENTAL METHODS

2.1. Sample Preparation

The sample was prepared by induction heating of a carbon crucible containing equimolar amounts of $CaCO_3$ (4N, Roc-Ric) and Y_2O_3 (4N, Hudson Lab) in a stream of 5% H_2S + 95% argon at 1600°C for 4 hr and then cooled to room temperature by switching off the furnace. The product was purple (violet) in color and had partly melted. That the resultant product (see below) is Y-poor relative to the starting materials suggests that Y must be lost to either the atmosphere or the vessel during the reaction.

2.2. Experimental Techniques

The specimen was analyzed by X-ray powder diffraction using a Guinier–Hägg camera. The positions of diffraction lines were calibrated using an internal standard of silicon (NBS No. 640). Transmission electron microscope (TEM) studies were performed on Siemens Elmiskop 102, JEOL 100CX and Philips EM430 electron microscopes. Energy dispersive spectroscopy was carried out on the Philips EM430 using a Si detector supported by a PV9900 analysis system. Specimens were ground under *n*-butanol, and a drop of the suspension was left to evaporate on carbon coated copper grids.

3. RESULTS

3.1. X-Ray Diffraction

The diffraction pattern was dominated by a strong set of broad lines corresponding to an *F*-centered cubic unit cell with $a \approx 5.66$ Å. Interpretation of these data was not possible without unit cell information obtained by electron diffraction from single crystal grains as discussed in Section 3.2 below. The set of strong, broad lines together with the weaker broad lines could all be indexed to a rhombohedral unit cell ($\mathbf{a}' = \frac{1}{2}(2\mathbf{a} + \mathbf{b} + \mathbf{c})$, $\mathbf{b}' = \frac{1}{2}(\mathbf{a} + 2\mathbf{b} + \mathbf{c})$, $\mathbf{c}' = \frac{1}{2}(\mathbf{a} + \mathbf{b} + 2\mathbf{c})$), $a' = 6.942(1)$ Å and $\alpha = 33.380(5)°$, which is only slightly distorted from cubic. These data are presented in Table 1 together with their relationship to the parent *F*-centered cubic unit cell. The relationship between the reciprocal lattices of the rhombohedral superstructure and that of the $Fm3m$ parent structure is given by $\mathbf{a}'^* = \frac{1}{2}(3, -1, -1)^* = (200)^* - \frac{1}{2}(111)^*$, $\mathbf{b}'^* = \frac{1}{2}(-1, 3, -1)^* = (020)^* - \frac{1}{2}(111)^*$, and $\mathbf{c}'^* = \frac{1}{2}(-1, -1, 3)^* = (002)^* - \frac{1}{2}(111)^*$. Note that reflections of the form $\mathbf{G} \pm \frac{1}{2}(111)^*$ are thereby allowed but not reflections of the form $\mathbf{G} \pm \frac{1}{2}(1\bar{1}1)^*$ etc.

TABLE 1
Powder Diffraction Data for the Rhombohedral Phase, $a = 6.942$ Å, $\alpha = 33.380°$

No.	dobs (Å)	dcalc (Å)	I/I_0	hkl_{rh}	hkl_{parent}
1.	6.562	6.549	15	111	
2.	3.401	3.401	12	001	
3.	3.268	3.275	11	222	111
4.	2.826	2.825	100	112	200
5.	2.593	2.594	2	221	
6.	2.178	2.178	4	232	
7.	2.001	2.001	70	233	220
8.	1.994	1.994	25	−110	220
9.	1.907	1.907	3	120	
10.	1.707	1.708	5	343	311
11.	1.703	1.703	3	123	311
12.	1.638	1.637	20	444	222
13.	1.629	1.629	2	220	
14.	1.586	1.587	2	443	
15.	1.472	1.472	1	342	
16.	1.413	1.412	15	242	400
17.	1.300	1.300	2	554	331
18.	1.266	1.265	33	354	420
19.	1.262	1.261	15	013	420
20.	1.157	1.157	22	565	422
21.	1.152	1.153	16	143	422

Apart from the broad lines there were also lines which were relatively weak, but quite sharp, and most could be indexed to a body-centered cubic structure with refined unit cell dimension $a = 8.327(4)$ Å. From the phase diagram and lattice parameter measurements of Flahaut *et al.* (6), it is clear that this bcc phase corresponds to the solid solution of Th_3P_4 type designated γ by Flahaut *et al.* (6). The remaining very weak lines corresponded to the strongest lines of CaY_2S_4 (JCPDS File No. 17-244). We estimate that these two minor phases, taken together, comprised less than 5% of the crystalline material. As the major focus of this paper is upon the sub-stoichiometric, NaCl related phase, however, we will from now on concentrate upon it.

3.2. *Electron Diffraction*

According to Flahaut *et al.* (6), the NaCl-type solid solution end member is $\sim Ca_{0.61}Y_{0.27}S$ from 1100 to 1400°C. Energy dispersive spectroscopy (EDS) of the cubic NaCL-type grains in our specimen, using $Ca_{0.125}Zr_{0.875}O_{1.875}$ as a standard, showed that the composition of all grains observed were homogeneous and gave a Ca/Y ratio of 5/4, i.e., $Ca_{0.45}Y_{0.36}S$, $Ca_5Y_4S_{11}$ or 71.4 mole% CaS. Note that there is little variation in the *K*-factors commonly used for calculating relative atomic proportions between adjacent elements in the periodic table (see Chapter 4 of Williams (18)) and hence $Ca_{0.125}Zr_{0.875}O_{1.875}$ (Zr and Y are neighboring elements in the periodic table) can be used as a standard. Flahaut *et al.* (6) report a cubic cell dimension for their end member composition of 5.663 Å at 1020°C and 5.651 Å at 1350°C, which fits quite nicely with our observed cell dimension of ~5.66 Å at 1600°C.

Given the cubic $Fm3m$ parent symmetry, it is clear that there can be four orientational variants or rhombohedral twins. As will be shown below, these orientational variants usually occur on a scale substantially smaller than the ~1-μm diameter area typically illuminated in selected area electron diffraction mode. Hence almost all of the selected area electron diffraction patterns (SADPs) shown below do not come from a single rhombohedral crystal. It is not, therefore, possible to index them with respect to a single resultant rhombohedral structure or, in general, even to know whether one, two, three, or all four orientation variants are contributing to the resultant SADP and in what proportion. All the orientation variants, however, do have in common the underlying NaCl-type parent structure. In what follows all diffraction patterns have therefore been indexed with respect to this underlying $Fm3m$, $a \sim 5.66$ Å, NaCl-type parent structure; i.e., the reader should be aware that the labeling from here on refers to the underlying cubic parent structure and not to the rhombohedral superstructure.

Figure 1 shows (a) ⟨001⟩, (b) ⟨011⟩, (c) ⟨125⟩, (d) ⟨013⟩, (e) ⟨111⟩, (f) ⟨123⟩, (g) ⟨012⟩, (h) ⟨112⟩, (i) ⟨114⟩, and (k) ⟨332⟩ type zone axis SADPs characteristic of this $Ca_5Y_4S_{11}$ phase. All SADPs have been indexed with respect to the underlying NaCl-type parent structure. These particular SADPs have been chosen to enable a comparison with those given in Fig. 2 of Ref. (9) for the sub-stoichiometric transition metal carbide $VC_{0.75}$. While there are significant differences, principally the existence of additional $\mathbf{G} \pm \frac{1}{2}\{111\}^*$ type satellite reflections in (b), (c), (d), (h), and (i), there are nonetheless also many similarities in the form of the spectacular diffuse intensity distributions characteristic of both of these deficit NaCl-type materials. Thus the diffuse intensity distributions in patterns (b), (d), (f), and (i) are very similar if not identical to those reported in Ref. (9). On the other hand, pattern (c) is significantly different. Patterns (a) and (e) are intermediate in that only part of the diffuse distribution present in the case of $VC_{0.75}$ remains in the case of $Ca_5Y_4S_{11}$. Thus, only two sides of the diffuse square characteristic of ⟨001⟩ SADPs of $VC_{0.75}$ remain in the case of $Ca_5Y_4S_{11}$. Similarly only two sides of the hexagon of diffuse intensity characteristic of ⟨111⟩ type zone axis SADPs of $VC_{0.75}$ remain in the case of $Ca_5Y_4S_{11}$. In the case of the ⟨112⟩ zone axis SADP (pattern (h)), the diffuse intensity distribution is closely related to that in the corresponding zone axis SADP of $VC_{0.75}$ except for the regions directly above the $\mathbf{G} \pm \frac{1}{2}\{111\}^*$ satellite reflections.

Sauvage and Parthe (10) have shown how the diffuse intensity distribution characteristic of $VC_{0.75}$ relates to a short-range ordering of carbon vacancies. The three-dimensional reciprocal space diffuse intensity distribution is shown to have cubic symmetry and to be closely related to the shape of the Fermi surface of a simple cubic metal (see Fig. 1 of Ref. (10)). In turn this is closely related to the so-called *P* minimal surface. The diffuse intensity distribution characteristic of $Ca_5Y_4S_{11}$, while related nonetheless has distinct differences. Complete characterization of this diffuse intensity distribution is beyond the scope of this paper. Further work along these lines, however, is in progress.

While it is very difficult to detect broken cubic symmetry in the underlying average structure cell parameters, particularly by means of electron diffraction, broken cubic symmetry is clearly visible in the diffuse distributions. Thus the diffuse distribution in the ⟨001⟩ zone axis SADP of Fig. 1(a) does not show fourfold symmetry nor does the diffuse distribution in the ⟨111⟩ zone axis SADP of Fig. 1 (e) show threefold symmetry. Similarly a detailed examination of reciprocal space shows that zone axes which should be equivalent for cubic symmetry can be quite distinct. Thus Fig. 2 shows three quite different ⟨112⟩ cubic parent type zone axis SADPs in addition to that shown in Fig. 1(h). Apart from the differences in the observed diffuse intensity distributions, there are also differences with respect to satellite reflections; i.e., the local space group symmetry is clearly not cubic. Thus

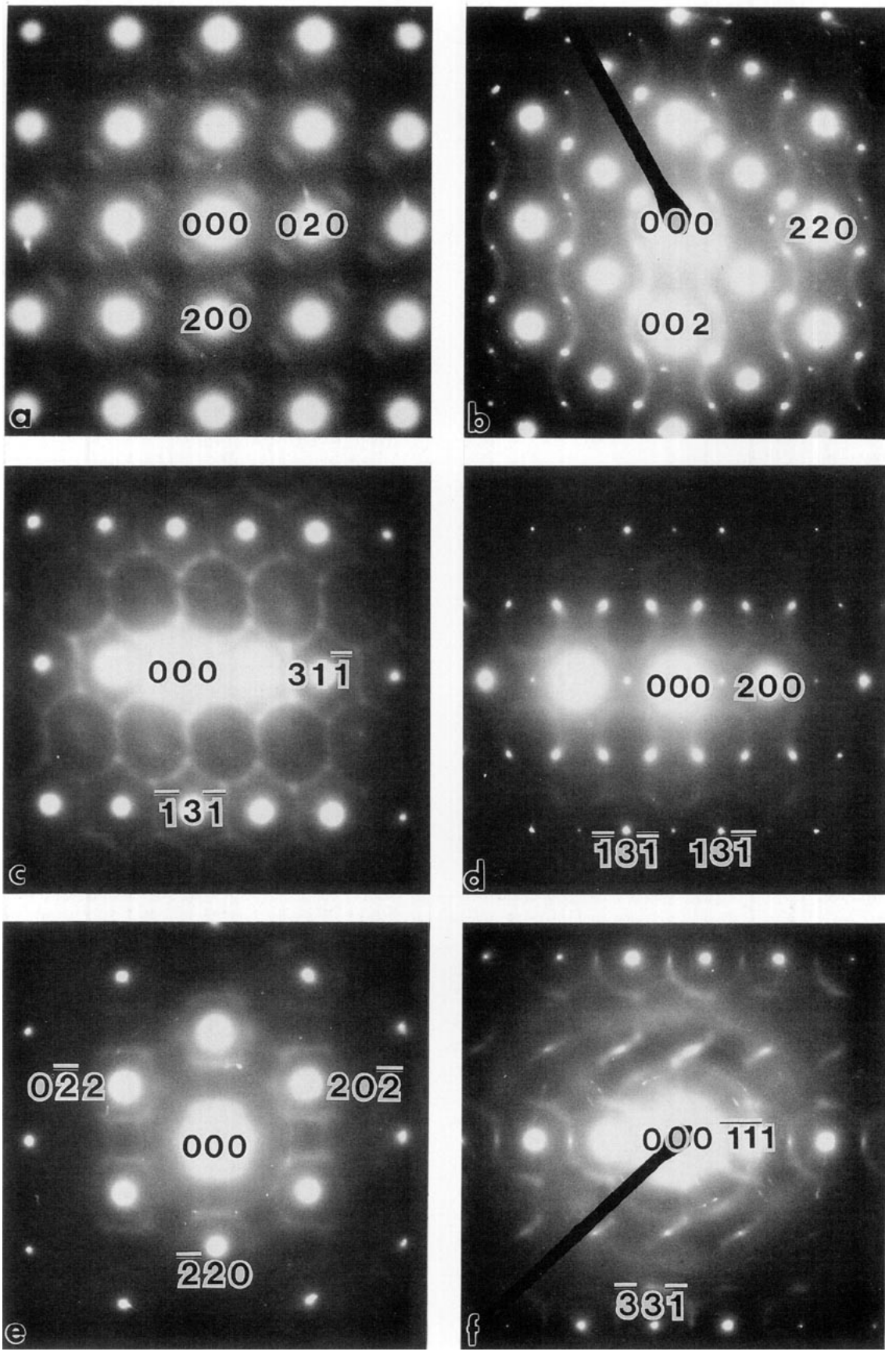

FIG. 1. Shows (a) ⟨001⟩, (b) ⟨011⟩, (c) ⟨125⟩, (d) ⟨013⟩, (e) ⟨111⟩, (f) ⟨123⟩, (g) ⟨012⟩, (h) ⟨112⟩, (i) ⟨114⟩, and (k) ⟨332⟩ type zone axis selected area electron diffraction patterns (SADPs) characteristic of this $Ca_5Y_4S_{11}$ phase. All SADPs have been indexed with respect to the underlying NaCl-type parent structure.

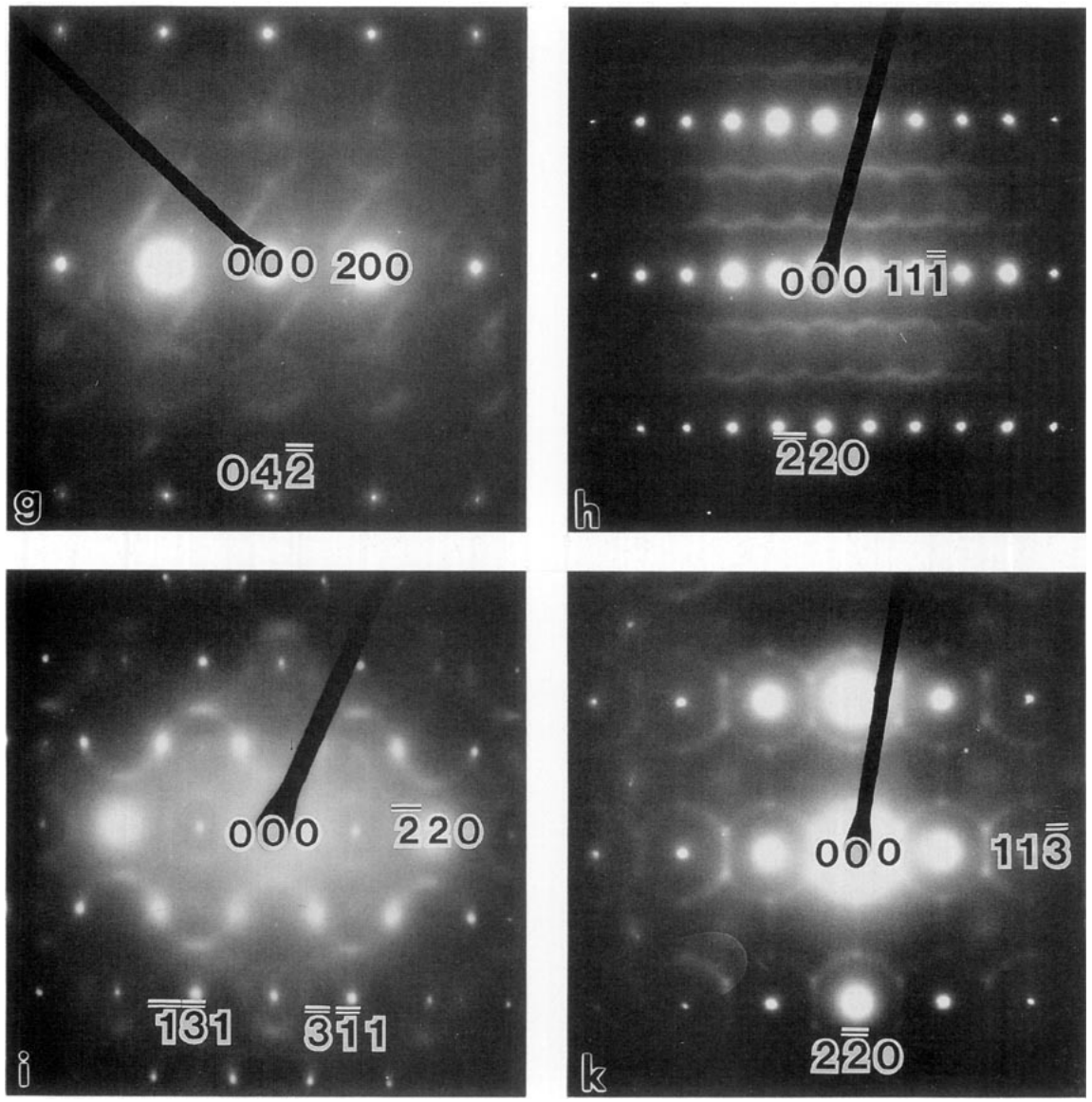

FIG. 1—*Continued.*

reflections of the form $\mathbf{G} \pm \frac{1}{2}(11\bar{1})^*$ (given the parent indexing used) exist in (a) (although somewhat streaked) and also weakly in (b) but not in (c). Similarly reflections of the form $\mathbf{G} \pm \frac{1}{2}(111)^*$ (note that $\frac{1}{2}(\bar{1}3\bar{1})^*$ is equivalent to $(020)^* - \frac{1}{2}(111)^*$) exist in (a) and (c) but not in (b). Thus at least two of the four distinct possible $\frac{1}{2}\{111\}^*$ modulations are present in (a).

The question as to how many of the four distinct possible $\frac{1}{2}\{111\}^*$ modulations are ever locally present in any one area is difficult to determine as only two of the four possible sets of satellite reflections corresponding to these modulations can ever be simultaneously present in the zero order Laue zone (ZOLZ) of major zone axis SADPs. Thus Fig. 3(c), for example, shows a typical ⟨110⟩ type zone axis microdiffraction pattern. Satellite reflections of the form $\mathbf{G} \pm \frac{1}{2}\{111\}^*$ and $\mathbf{G} \pm \frac{1}{2}\{11\bar{1}\}^*$ are simultaneously present. Notice, however, that they do not have equal intensity. Furthermore, the relative intensities of these two sets of satellite reflections clearly altered as the incident convergent beam probe was moved around the grain, suggesting that the presence of both sets of satellite reflections in Fig. 3(c), must be due to twinning. This was confirmed by means of satellite dark field (SDF) imaging. Thus Fig. 3(b) shows a $\frac{1}{2}\{111\}^*$ SDF image while Fig. 3(a) shows the corresponding bright field (BF) image. Only those regions which contain satellite reflections of the form $\mathbf{G} \pm \frac{1}{2}\{111\}^*$ light up in (b). The dark regions in (b) contain satellite reflections of the form $\mathbf{G} \pm \frac{1}{2}\{11\bar{1}\}^*$. For this particular grain the twinning is on the scale of ~0.2 μm. Often, however, it is on an even finer scale.

Given cubic parent symmetry, one might expect antiphase boundaries (apbs) to occur, across which the

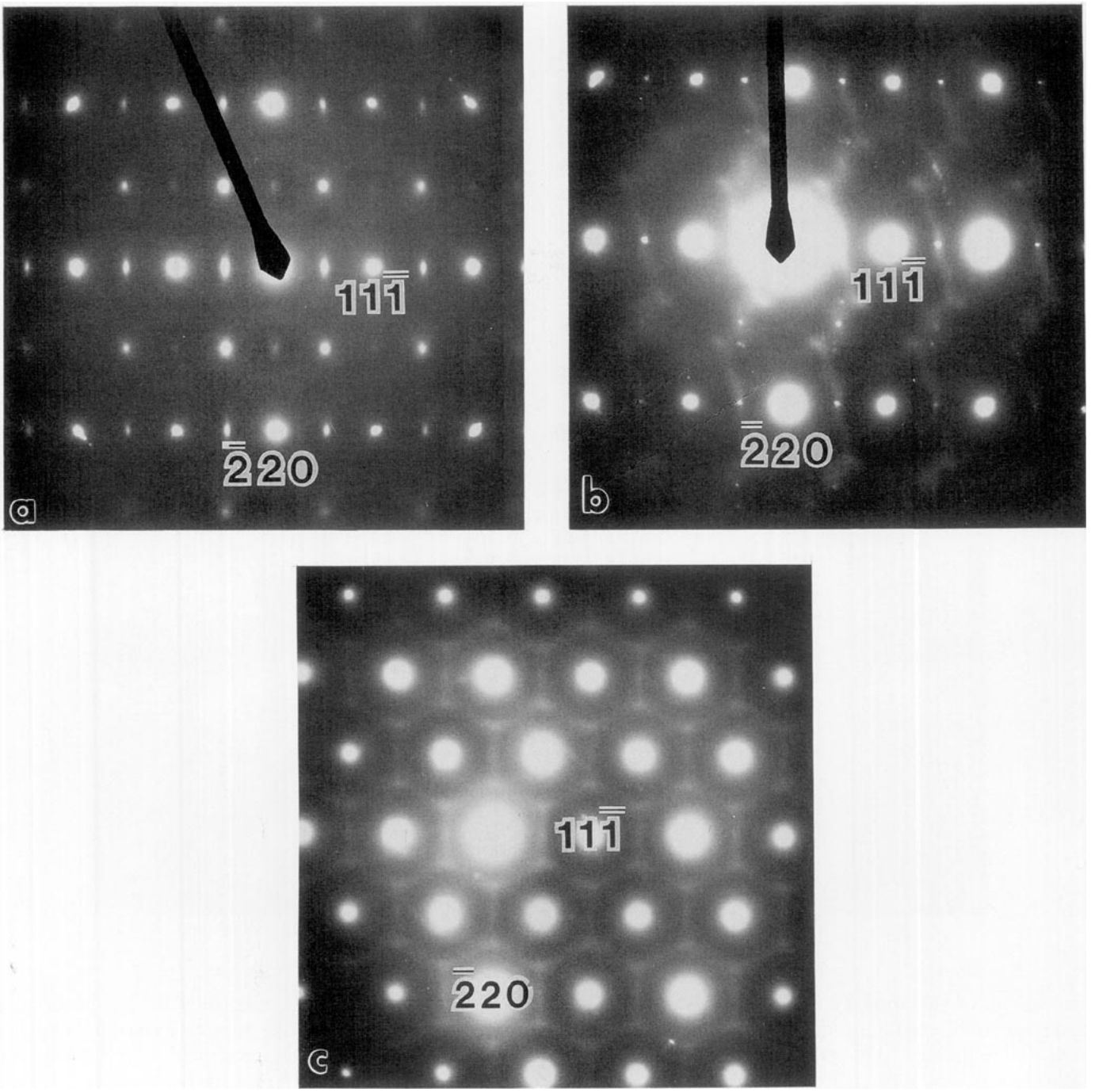

FIG. 2. Shows three quite distinct ⟨112⟩ type zone axis SADPs in addition to that shown in Fig. 1(h). Again all SADPs have been indexed with respect to the underlying NaCl-type parent structure. Zone axes which should be equivalent for cubic symmetry are quite clearly distinct.

$\frac{1}{2}\{111\}^*$ type modulations of the underlying average structure are phase shifted by 180°. Contrast of this type can be seen in the $\mathbf{G} \pm \frac{1}{2}\{111\}^*$ SDF image shown in Fig. 4(a). The corresponding microdiffraction pattern and BF image are shown in Fig. 4(b) and (c), respectively. The zone axis orientation is tilted slightly away from an ⟨031⟩ orientation in such a way that the $\{002\}^* + \frac{1}{2}\{111\}^* = \frac{1}{2}\{11\bar{3}\}^*$ reflection is strongly excited. Under such diffraction conditions, the apb contrast is also clearly visible in the BF image as shown in (c). However, this BF contrast can be made to disappear by slightly tilting the incident beam orientation such that $\mathbf{G} \pm \frac{1}{2}\{111\}^*$ satellite reflections are no longer strongly excited as shown in (d).

Possibly the best way of detecting the number of $\frac{1}{2}\{111\}^*$

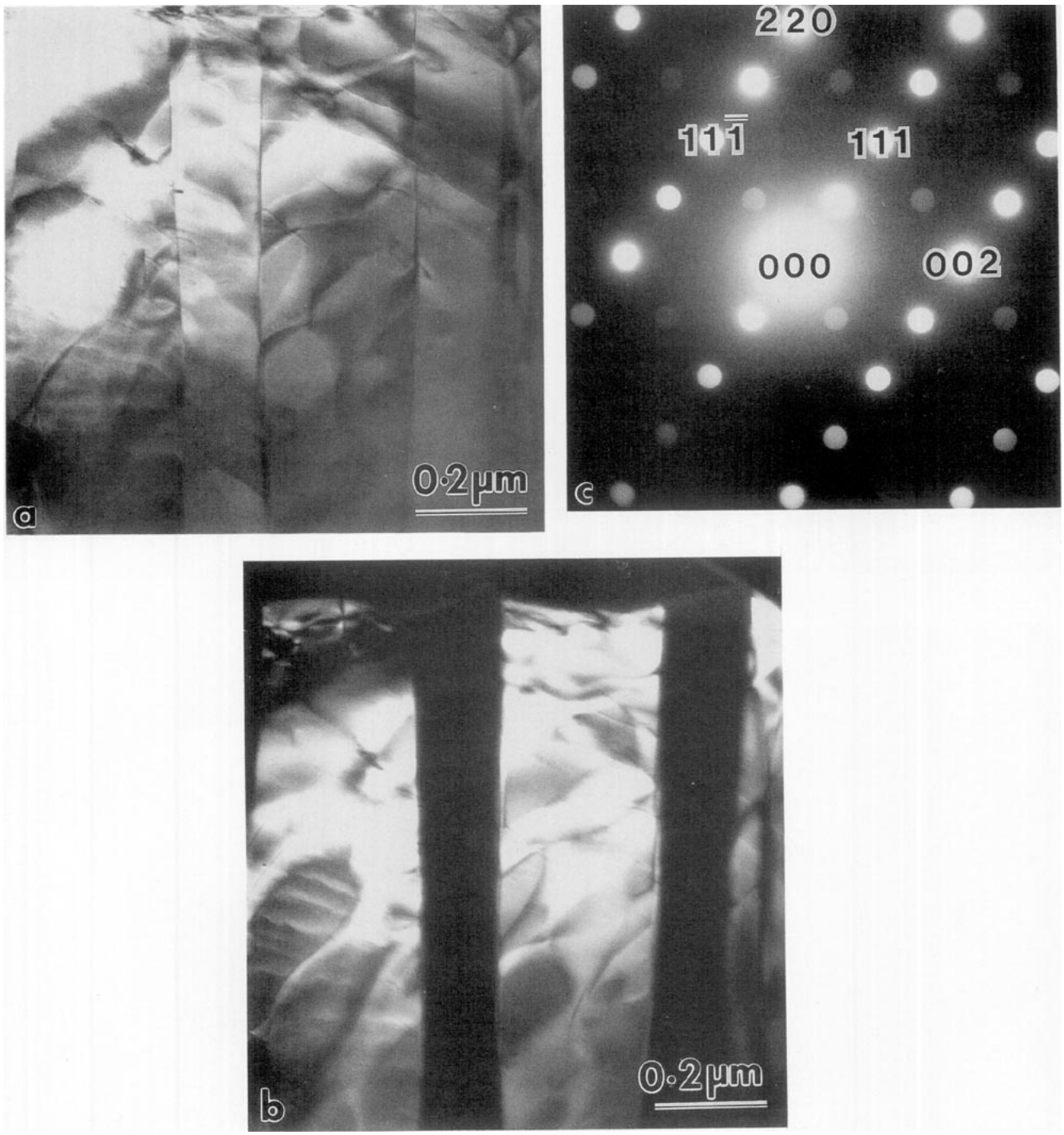

FIG. 3. Satellite reflections of the form $\mathbf{G} \pm \frac{1}{2}\{111\}^*$ and $\mathbf{G} \pm \frac{1}{2}\{111\}^*$ are simultaneously present in the typical $\langle 110 \rangle$ type zone axis microdiffraction pattern shown in (c). The corresponding $\frac{1}{2}\{111\}^*$ satellite dark field (SDF) image and bright field (BF) image are shown in (b) and (a), respectively. Only those regions which contain satellite reflections of the form $\mathbf{G} \pm \frac{1}{2}\{111\}^*$ light up in (b). The dark regions in (b) contain satellite reflections of the form $\mathbf{G} \pm \frac{1}{2}\{111\}^*$. For this particular grain the twinning is on the scale of ~0.2 μm.

modulations present in any one local area however is by inspection of superlattice higher order Laue zone (HOLZ) rings as can be seen in the $\langle 001 \rangle$ and $\langle 111 \rangle$ type zone axis SADPs shown in Fig. 5. The positioning of the reciprocal lattice mesh in the superlattice HOLZ ring with respect to that in the ZOLZ gives the number of $\frac{1}{2}\{111\}^*$ modulations locally present. Thus only reflections of the form $\{hk0\}^* \pm \frac{1}{2}\{\bar{1}\bar{1}1\}^*$ (arrowed in Fig. 5(a)) are present in the superlat-

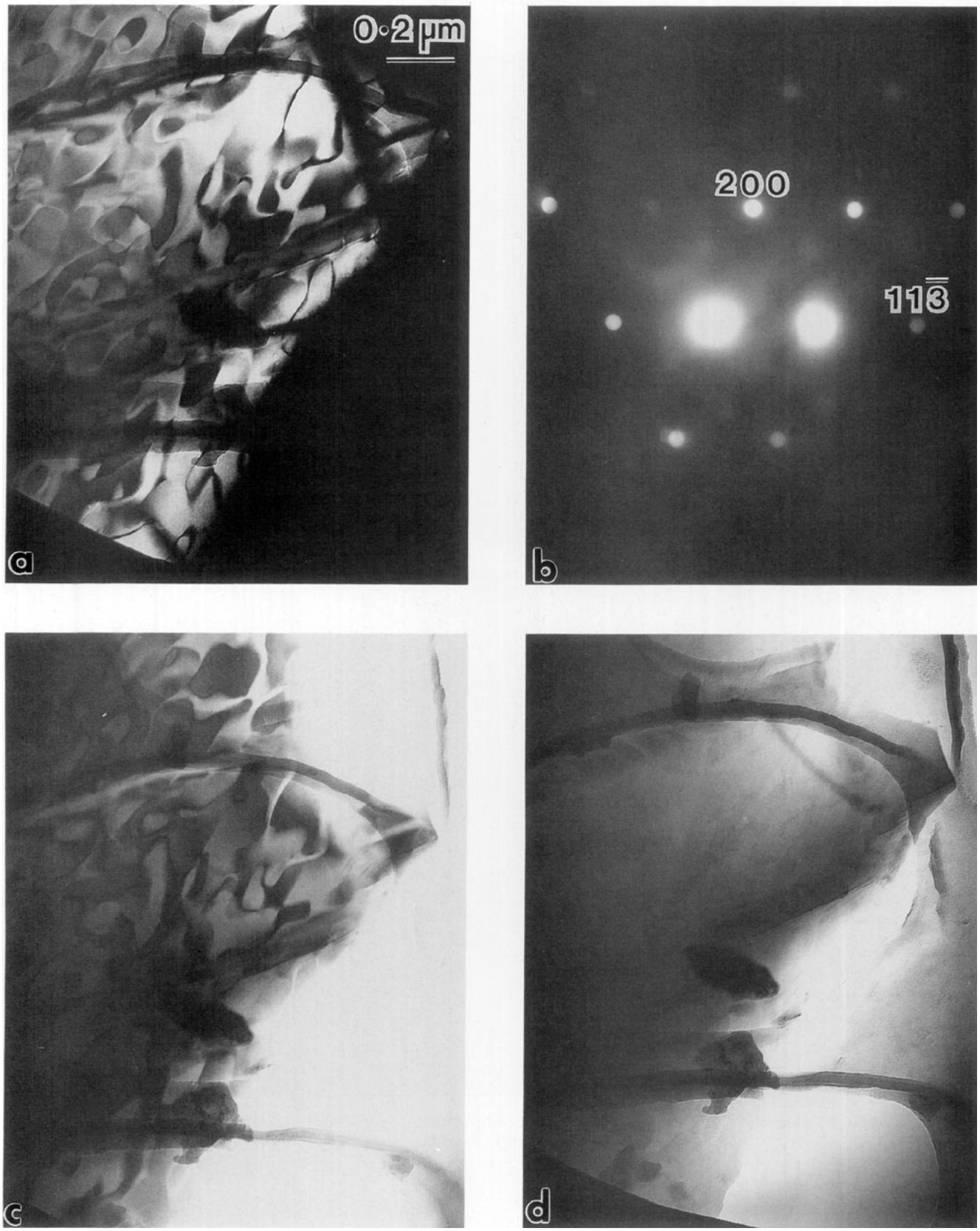

FIG. 4. Given cubic parent symmetry, one might expect antiphase boundaries (apbs) to occur, across which the $\frac{1}{2}\{111\}^*$ type modulations of the underlying average structure are phase shifted by 180°. Contrast of this type can be seen in the $\mathbf{G} \pm \frac{1}{2}\{111\}^*$ SDF image shown in (a). The corresponding microdiffraction pattern and BF image are shown in (b) and (c), respectively. The zone axis orientation is tilted slightly away from an $\langle 031 \rangle$ orientation in such a way that the $\{00\bar{2}\}^* + \frac{1}{2}\{111\}^* = \frac{1}{2}\{11\bar{3}\}^*$ reflection is strongly excited. Under such diffraction conditions, the apb contrast is also clearly visible in the BF image as shown in (c). However, this BF contrast can be made to disappear by slightly tilting the incident beam orientation such that $\mathbf{G} \pm \frac{1}{2}\{111\}^*$ satellite reflections are no longer strongly excited as shown in (d).

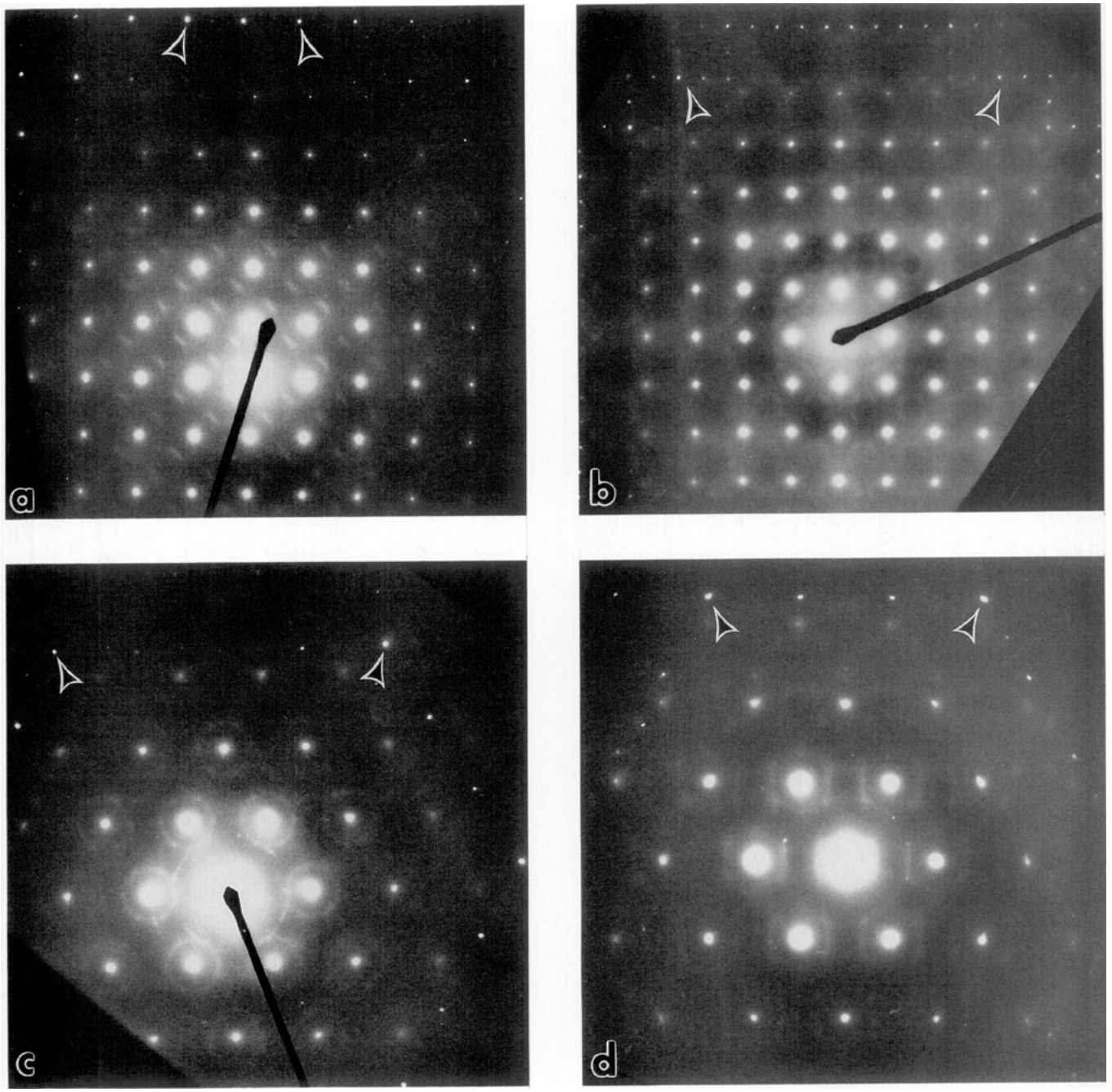

FIG. 5. Shows typical ⟨001⟩ ((a) and (b)) and ⟨111⟩ ((c) and (d)) type zone axis SADPs. The positioning of the reflections in the superlattice HOLZ rings (arrowed) with respect to those in the ZOLZ gives the number of $\frac{1}{2}\{111\}^*$ modulations locally present.

tice HOLZ ring—we have assumed the same indexing of the parent reflections as given in Fig. 1(a). ⟨001⟩ type zone axis SADPs were often of this form, i.e., only one of the four possible $\frac{1}{2}\{111\}^*$ modulations locally present. On quite a few occasions, however, patterns such as that shown in Fig. 5(b) were found. There is a doubled density of reflections in the FOLZ ring of Fig. 5(b) along both the horizontal and vertical directions as compared to that in the FOLZ ring of Fig. 5(a)—hence there is an overall fourfold increased density of reflections. This fourfold increased density of reflections in the superlattice HOLZ ring (arrowed) implies that all four $\frac{1}{2}\{111\}^*$ modulations are present within the illuminated region of crystal. Note that the diffuse distribution within the ZOLZ has also changed and is now in the form of diffuse squares very similar to that observed in $VC_{0.75}$. It is of course difficult to rule out the possibility that this may be due to twinning.

In any event, however, it is clear that in the majority

of cases only one of the four possible $\frac{1}{2}\{111\}^*$ modulations is ever locally present thus reducing the space group symmetry from cubic to rhombohedral (probably either $R3m$ or $R\bar{3}m$). This is confirmed by the $\langle 111\rangle$ type zone axis SADPs shown in (c) and (d). The $\langle 111\rangle$ type zone axis SADP shown in (c) corresponds to the rhombohedral [111] zone axis and only contains reflections of the form $\mathbf{G} \pm \frac{1}{2}\{111\}^*$ in the superlattice HOLZ ring (arrowed). Note that the diffuse distribution in the ZOLZ of (c) is now in the form of circles rather than in the form of two sides of a diffuse hexagon as is more commonly found (see (d)). When an SADP from a single rhombohedral domain can be obtained and when not looking down the rhombohedral [111] zone axis, $\langle 111\rangle$ zone axis SADPs typically look like that shown in (d). Again only one type of $\frac{1}{2}\{111\}^*$ modulation is present in the superlattice HOLZ ring.

4. DISCUSSION

4.1. *Structural Degrees of Freedom Associated with the Single-q = $\frac{1}{2}\{111\}^*$ Modulation*

Having established that $Ca_5Y_4S_{11}$ can be described in terms of an $Fm3m$, NaCl-type parent structure modulated by a single- $\mathbf{q} = \frac{1}{2}\{111\}^*$ modulation, it is now necessary to describe the additional associated structural degrees of freedom. Given an $Fm3m$, NaCl-type parent structure, the average atomic scattering factor of the metal atom sites is given by $\bar{f}_M = \frac{1}{11}(5f_{Ca} + 4f_Y)$. We make the assumption that the $\mathbf{q} = \frac{1}{2}\{111\}^*$ modulation is associated with cation vacancy ordering and associated structural relaxation. As shown by Franzen and co-workers (3, 19), compositional modulation of this average metal atom occupancy can only be associated with the totally symmetric irreducible representation of the modulation wave-vector $\mathbf{q} = \frac{1}{2}(111)^*$. Under the assumption that the only displacive modulation to occur will transform with the same irreducible representation as this compositional modulation, the resultant space group symmetry would be $R\bar{3}m$ with only two additional structural degrees of freedom as shown in Fig. 6.

The first, δf_M, allows neighboring (111) metal atom planes to alternate in average occupancy from $(\bar{f}_M + \delta f_M)$ to $(\bar{f}_M - \delta f_M)$, while the second is an associated [111] shift of the (111) planes of S atoms. Determination of the absolute magnitude of these two structural degrees of freedom from powder data will be difficult, however, particularly given the common occurrence of antiphase boundaries as shown in Fig. 4. The compositional degree of freedom can be thought of as having two components, the first controlling the average vacancy concentration in the two distinct (111) metal atom planes and the second the extent of any Ca/Y segregation. It is not, however, possible to determine these two components separately from Bragg diffraction data, as the additional superstructure peaks only contain information as to the average scattering power of the two structurally distinct (111) metal atom planes.

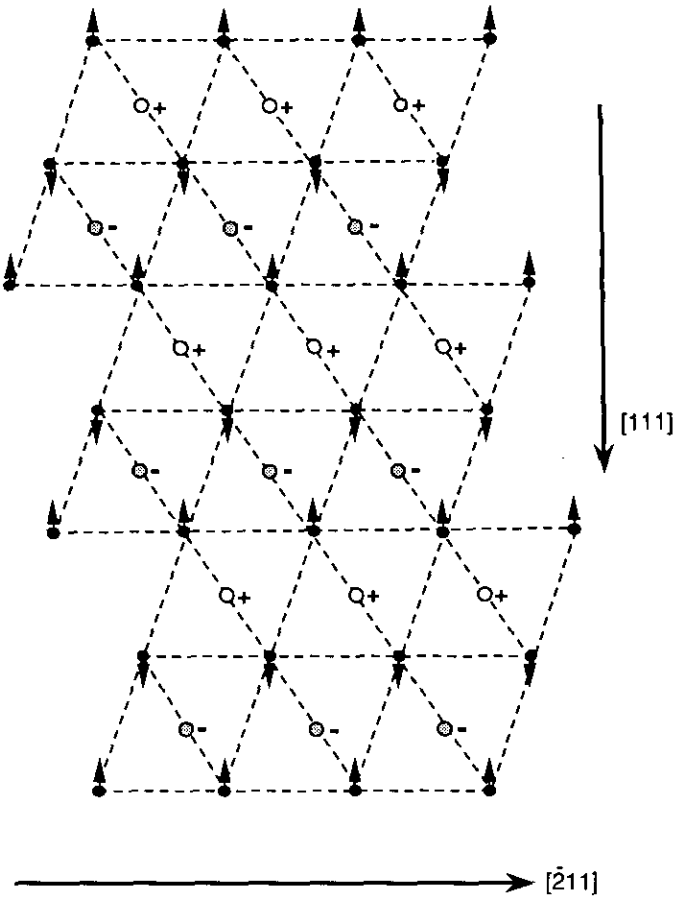

FIG. 6. Shows an [0, −1, 1] projection of the parent NaCl-type structure along with the additional structural degrees of freedom associated with the totally symmetric, mixed compositional, and displacive $\mathbf{q} = \frac{1}{2}(111)^*$ modulation thereof. The larger circles represent the metal atom sites while the smaller circles represent the sulfur atom sites. The projected sulfur atom array is given by the dashed lines and the parent [111] and [−2, 1, 1] vectors are marked. The + and − signs associated with alternate (111) planes of metal atoms represent the fact that neighboring (111) metal atom planes are now allowed to alternate in average occupancy from $(\bar{f}_M + \delta f_M)$ to $(\bar{f}_M - \delta f_M)$. The arrows represent the allowed relaxation of the sulfur atom array associated with such compositional ordering.

4.2. *The Characteristic Diffuse Distribution*

If we assume complete vacancy segregation (and ignore any Ca/Y ordering), as has been assumed in the apparently isomorphous case of $Sc_{0.8}S$ below 700°C (3, 15, 19), this would imply a vacancy concentration of $\frac{4}{11}$ in every alternate metal atom plane. The spectacular diffuse distribution which accompanies the Bragg reflections must then result from the metal vacancy distribution within and among such (111) metal atom planes. The sharpness of the

diffuse features in certain directions of reciprocal space clearly implies that the vacancy distribution is far from random.

The similarity of the diffuse distributions in many of the zone axis SADPs shown in Fig. 1 to those characteristic of VC_{1-x} (9, 10) strongly suggests a closely related structural origin. In this latter case, the diffuse distribution was shown to result from vacancy short-range order—in particular a requirement that vacancies should repel each other as far as possible. Each V atom had, as far as possible, 5, rather than 4 or 6, C atom nearest neighbors. For $Ca_5Y_4S_{11}$, each metal atom will be surrounded by 6 S atoms, whereas each S atom will be surrounded on average by 4.91 metal atoms. Calculation of bond valence sums (20) for S in the parent structure, i.e., in the absence of Ca/Y ordering and associated structural relaxation, suggest that the S's would prefer fivefold coordination to either four- or sixfold coordination and hence provides something of a chemical justification for vacancy short-range ordering. Long-range vacancy ordering along the [111] direction, in the case of $Ca_5Y_4S_{11}$, could be expected to strongly affect the type and frequency of occurrence of the octahedral metal atom clusters surrounding each S atom (10, 21) responsible for the detailed shape of the observed diffuse distribution. Further consideration, however, is beyond the scope of the present paper.

5. CONCLUSION

In conclusion, a TEM study of the metal atom deficient, NaCl-related $Ca_5Y_4S_{11}$ structure shows that its reciprocal lattice contains extra satellite reflections, at $\mathbf{G} \pm \frac{1}{2}\{111\}^*$, in addition to the strong Bragg reflections, $\mathbf{G}$, of the underlying $Fm3m$, NaCl-type average structure. Satellite dark field imaging in conjunction with the observation of superlattice HOLZ rings in appropriate SADPs strongly suggests that only one out of the four possible modulation wave-vectors of the form $\frac{1}{2}\{111\}^*$ locally exists. The resultant rhombohedral superstructure appears to be isomorphous to that previously reported for $Sc_{0.80}S$ below 700°C (17). In addition, its reciprocal lattice exhibits a spectacular diffuse intensity distribution which shows many similarities but also significant differences to that previously reported in sub-stoichiometric transition metal carbides and nitrides.

REFERENCES

1. H. F. Franzen and R. T. Tuenge, *J. Chem. Phys.* **65,** 2400 (1976).
2. H. Franzen, "Lecture Notes in Chemistry." Springer-Verlag, Heidelberg, 1982.
3. H. F. Franzen and J. C. W. Folmer, *J. Solid State Chem.* **51,** 396 (1984).
4. J. A. Hodges, G. Jehanno, D. Debray, F. Holtzberg, and M. Loewenhaupt, *J. Phys.* **43,** 961 (1982).
5. L. C. Otero-Diaz, A. R. Landa-Canovas, and B. G. Hyde, *J. Solid State Chem.* **89,** 237 (1990).
6. J. Flahaut, L. Domange, and M. Patrie. *C.R. Acad. Sci.* **251,** 2535 (1960); *Bull. Soc. Chim. Fr.*, 105 (1961).
7. M. Patrie and J. Flahaut, *C.R. Acad. Sci., Ser. 2* **264,** 395 (1967).
8. J. Flahaut, *in* "Handbook on the Physics and Chemistry of Rare Earths" (K. A. Gschneider and L. Eyring, Eds.), Vol. 4, p. 1. North–Holland, Amsterdam, 1979.
9. J. Billingham, P. S. Bell, and M. H. Lewis, *Acta Crystallogr., Sect. A* **28,** 602 (1972).
10. M. Sauvage and E. Parthe, *Acta Crystallogr., Sect. A* **28,** 607 (1972).
11. J. Billingham, P. S. Bell, and M. H. Lewis, *Philos. Mag.* **25,** 661 (1972).
12. C. H. de Novion, R. Lorenzelli, and P. Costa. *C.R. Acad. Sci.* **263,** 775 (1966).
13. A. Tomas, M. Robert, and M. Guittard, *Mater. Res. Bull.* **23,** 507 (1988).
14. M. Patrie, J. Flahaut, and L. Domange, *Rev. Hautes Temp. Refract.* **2,** 187 (1965).
15. H. F. Franzen and J. A. Merrick, *J. Solid State Chem.* **33,** 371 (1980).
16. B. R. Conard and H. F. Franzen, *in* "The Chemistry of Extended Defects in Non-metallic Solids" (M. O'Keeffe and L. Eyring, Eds.). North–Holland, Amsterdam, 1970.
17. H. F. Franzen, R. J. Tuenge, and L. Eyring, *J. Solid State Chem.* **49,** 206 (1983).
18. D. B. Williams, "Practical Analytical Electron Microscopy in Materials Science." Philips Electronic Instruments Inc., New Jersey, 1983.
19. H. F. Franzen, "Physical Chemistry of Inorganic Crystalline Solids," Springer-Verlag, Heidelberg, 1986.
20. N. E. Brese and M. O'Keeffe, *Acta Crystallogr., Sect. B* **47,** 192 (1991).
21. R. de Ridder, G. van Tendeloo, D. van Dyck, and S. Amelinckx, *Phys. Status Solidi B* **38,** 663 (1976).